Wang *et al. Chem Synth* 2024;4:27
DOI: 10.20517/cs.2023.60

Chemical Synthesis

Research Article

Open Access

Graphene oxide membranes using MOF@Chitosan core-shell nanoparticles as dual modulators for dye separation

Xingying Wang[1,#], Yongmei Guo[2,#,*], Xiaolei Cui[1,#], Zhikun Wang[3], Zhihan Zhang[1], Lubomira Tosheva[4], Hailing Guo[1,*]

[1]College of Chemical and Chemical Engineering, China University of Petroleum (East China), Qingdao 266580, Shandong, China.
[2]Fujian Key Laboratory of Novel Functional Textile Fibers and Materials, Minjiang University, Fuzhou 350108, Fujian, China.
[3]School of Materials Science and Engineering, China University of Petroleum (East China), Qingdao 266580, Shandong, China.
[4]Department of Natural Sciences, Manchester Metropolitan University, Manchester M1 5GD, UK.
[#]Authors contributed equally.

[*]**Correspondence to:** Prof. Yongmei Guo, Fujian Key Laboratory of Novel Functional Textile Fibers and Materials, Minjiang University, No. 200 Xiyuangong Road, Minhou County, Fuzhou 350108, Fujian, China. E-mail: yongmeiguo@mju.edu.cn; Prof. Hailing Guo, College of Chemical and Chemical Engineering, China University of Petroleum (East China), No.66 Changjiang West Road, Huangdao District, Qingdao 266580, Shandong, China. E-mail: guohl@upc.edu.cn

How to cite this article: Wang X, Guo Y, Cui X, Wang Z, Zhang Z, Tosheva L, Guo H. Graphene oxide membranes using MOF@Chitosan core-shell nanoparticles as dual modulators for dye separation. *Chem Synth* 2024;4:27. https://dx.doi.org/10.20517/cs.2023.60

Received: 27 Nov 2023 **First Decision:** 22 Jan 2024 **Revised:** 24 Mar 2024 **Accepted:** 16 Apr 2024 **Published:** 14 May 2024

Academic Editors: Jin Xie, Guangshan Zhu **Copy Editor:** Pei-Yun Wang **Production Editor:** Pei-Yun Wang

Abstract

Graphene oxide (GO) membranes hold significant promise for the water purification. However, they also face the problem of structural swelling, which limits their use in water treatment applications. In this work, a novel dual-modulated core-shell metal-organic framework@Chitosan (MOF@CS) was successfully synthesized and used as an intercalation cross-linker to optimize the interlayer spacing and stability of GO membranes. Molecular dynamics simulation confirms that MOF@CS, acting as an intercalator, accelerates the water diffusion rate within the channels of the GO layer compared to a pure GO layer. At the same time, Fourier Transform Infrared Spectroscopy analysis reveals that MOF@CS serves as a cross-linker for covalently cross-linking the GO layer. The nanofiltration performance and stability of the improved MOF@CS-GO composite membranes were significantly enhanced. Compared to the pure GO membranes, the MOF@CS-GO composite membranes exhibited enhanced Congo red rejection rates (from 76.5% to 95.6%) while maintaining a high pure water flux (34.5 $L \cdot m^{-2} \cdot h^{-1} \cdot bar^{-1}$) and good structural stability (stable dye removal performance over 120 h). This dual regulation strategy is expected to

effectively solve the swelling problem of GO membranes in aqueous media and open up avenues for advancing their performance.

Keywords: Metal-organic framework, graphene oxide membrane, dual modulators, core-shell MOF@CS, dye separation

INTRODUCTION

Water is an essential resource for human life[1]. In recent years, the rapid growth of the textile industry has caused a significant discharge of wastewater from printing and dyeing, resulting in serious water pollution[2]. Organic dyes in water pose a severe threat to human health due to their high toxicity, mutagenicity, and carcinogenicity[3,4]. Therefore, developing high-performance dye removal technologies is an essential task in addressing the current water pollution problem[5]. Conventional dye separation methods, such as adsorption[6], coagulation, extraction, and biodegradation, are ineffective in terms of energy consumption[7]. Membrane separation technology is becoming a more energy-efficient means of water purification[8]. Achieving efficient dye separation heavily relies on using membrane materials possessing exceptional selectivity, permeability, and stability[9-12].

In recent years, graphene oxide (GO) has gained significant popularity as a membrane material for water treatment owing to its notable attributes such as high specific surface area and adjustable physicochemical properties[13]. The abundance of functional oxygen-containing groups on the surface and edges of GO membranes opens up the exciting potential for customizing and engineering them to achieve selective separation of specific dyes[14,15]. In general, GO membranes are composed of atomically thick GO nanosheets, assembled by hydrogen and π–π bonds, forming a layered stack structure[16,17]. Their transport channels are mainly formed by irregular folds[18], layer stacking[19], and structural defects. However, the stacking of GO nanosheets is dense, resulting in narrow interlayer channels, which affects the permeation flux[20-23]. Additionally, when GO nanosheets are in an aqueous solution, the hydration of the oxygen-containing functional groups on the surface breaks the hydrogen bonds between the sheets, causing swelling and disintegration of the GO membrane, thereby affecting its stability[24]. Therefore, obtaining a GO-based membrane with high stability, selectivity, and permeability remains a challenge.

Recently, intercalation, cross-linking, modification, and thickness adjustment have been used to improve the separation properties of GO membranes. Among them, intercalation is a controllable method to adjust the distance between GO membrane layers[25], and the selection of intercalating agents is crucial. Metal-organic frameworks (MOFs), as emerging porous crystalline materials, have been widely studied for their high porosity, designable structure, and adjustable pore size, which allows them to accurately regulate the GO layer spacing[26-28]. The introduction of MOFs into graphene nanosheets to form hybrid structures has recently attracted attention[29,30]. For example, Jiang *et al.* added FECUBDC bimetallic MOFs to GO nanosheets, which increased the interlayer spacing of the GO composite membrane and improved the efficiency of dye wastewater treatment[31]. In a similar study, Zeng *et al.* enhanced the membrane separation performance by embedding PAA@UiO-66-NH_2 between GO sheets through vacuum filtration self-assembly[32]. Although the introduction of MOFs has improved the performance of GO membranes, interface compatibility and GO swelling issues still exist due to the weak bonding between MOFs and GO[33]. One effective strategy to enhance the stability of GO layers is to introduce cross-linking agents. Chitosan (CS), with its high stability and ultra-high dye adsorption capacity, is a good choice for a cross-linking agent[34,35]. For example, Lu *et al.* constructed CS-GO/polyacrylonitrile (PAN) nanofiber membranes by grafting CS onto GO. The CS, as a cross-linking agent, can form strong bonds with GO, improving the stability and dye adsorption capacity of the membrane[36]. However, the cross-linking agent alone tends to

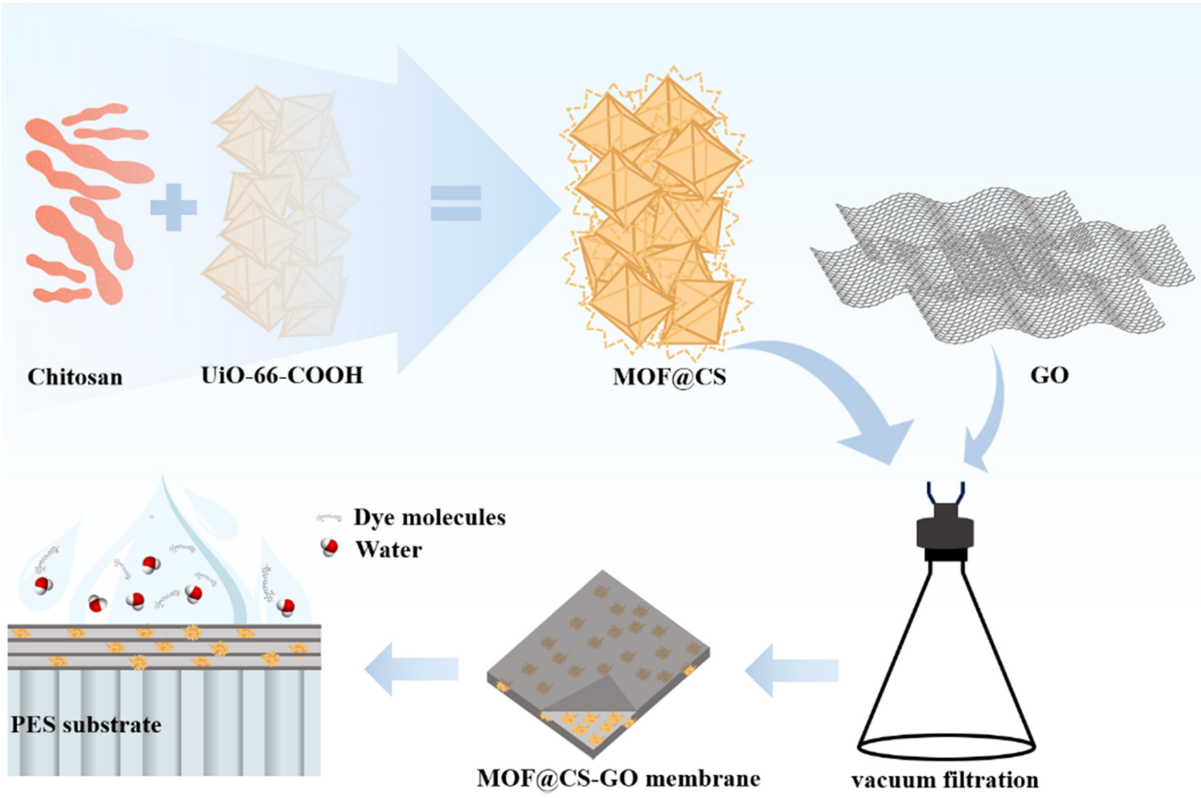

Scheme 1. Preparation of the MOF@CS-GO membrane. MOF@CS: Metal-organic framework@Chitosan; GO: Graphene oxide.

reduce the GO layer spacing, resulting in a lower flux[37]. Also, it is difficult to form an ordered layer spacing, which affects the screening capacity of the membrane[38]. Therefore, the rational design of the coupling of intercalating and cross-linking agents is of great significance for improving the performance of GO membranes.

In this work, a novel dual-modulated core-shell MOF@CS was successfully synthesized and utilized as an intercalation-cross-linker agent to optimize the interlayer spacing and stability of GO membranes [Scheme 1]. The abundant carboxyl groups on UiO-66-COOH and amino groups on CS can strongly interact to form a stable core-shell structure. On the one hand, the porous structure of MOF@CS core-shell nanoparticles is used to effectively expand the interlayer spacing between GO layers, providing a fast water transport channel. Further, the amino groups on CS can be chemically cross-linked with GO, which can greatly enhance the membrane stability. The GO membrane doped with MOF@CS core-shell nanoparticles prepared in this study has high water permeability and dye rejection. This strategy is expected to minimize the swelling of GO membranes and open up avenues for advancing the GO membrane performance.

EXPERIMENTAL

Chemicals

Polyethersulfone (PES) with a pore size of 0.1 μm was provided by Haiyan New Oriental Plastics Technology Co. GO (thickness of 0.8-1.2 nm) was purchased from the Institute of Coal Chemistry. CS and 1,2,4-benzenetricarboxylic acid ($C_9H_6O_6$, 98%) were provided by Aladdin Chemical Company. Zirconium chloride ($ZrCl_4$, 99.95%) was supplied by Strem Chemical. N, N-dimethylformamide (DMF, ≥ 99.5%), acetic acid (HAc, ≥ 99.5%), crystalline violet (CV, 99%), methylene blue (MB, 98%), and Congo red (CR, 99%) were derived from Sinopharma Chemicals.

Synthesis of UiO-66-COOH nanoparticles

UiO-66-COOH nanoparticles were prepared using the method reported previously[39]. Typically, 0.65 g $ZrCl_4$, 7.56 g deionized water, and 0.557 g 1,2,4-benzenetricarboxylic acid were added to 160 mL DMF. The obtained solution was kept in an oven at 120 °C for 24 h. After cooling the mixture to room temperature, the precipitate was collected through centrifugation. The UiO-66-COOH nanoparticles obtained were washed several times with methanol and deionized water.

Synthesis of MOF@CS core-shell nanoparticles

The dispersion of UiO-66-COOH was prepared by directly diluting the UiO-66-COOH solid collected after centrifugal. A portion of UiO-66-COOH water dispersion was transferred to a beaker. Twice the amount of CS powder was incorporated into the beaker, which was then diluted with 40 mL of deionized water. To completely dissolve and disperse the CS, 2-3 drops of acetic acid were added to the beaker. After stirring for 24 h, the solution was centrifuged and diluted with deionized water to obtain 0.1 wt% suspension of MOF@CS core-shell nanoparticles. The suspension was stirred for 6 h before storage.

Preparation of MOF@CS-GO composite membranes

GO suspension with a concentration of 0.025 mg·mL^{-1} was obtained by adding GO to deionized water. Then, 2 mL of the 0.1 wt% MOF@CS dispersion was diluted to 20 mL to obtain 0.01 wt% MOF@CS dispersion. The two suspensions were mixed according to the conditions provided in Table 1 and sonicated to form a homogeneous mixture. The MOF@CS-GO composite membranes were prepared on macropore PES substrates by vacuum filtration for 10 min. Finally, the MOF@CS-GO composite membranes were heated at 60 °C for 6 min to enhance the cross-linking between GO and MOF@CS. In addition, MOF/CS/GO composite membranes were prepared by physically mixing equal proportions of CS and MOF.

Characterizations

UiO-66-COOH and MOF@CS core-shell nanoparticles were subjected to X-ray diffraction (XRD, Bruker D8 Advance) analysis to ascertain their structural characteristics. Scanning electron microscopy (SEM, JEOL 7900F) and scanning transmission electron microscopy (STEM, FEI Talos F200×200 kV) were used to observe the morphology of the MOF@CS core-shell nanoparticles and MOF@CS-GO composite membranes. Atomic force microscopy (AFM, SMP-9700, Shimadzu) characterized the roughness of the membranes. Attenuated Total Reflection Fourier Transform Infrared Spectroscopy (ATR-FTIR, IRTracer-100, Shimadzu) further studied the membrane structure. The surface hydrophilicity of the MOF@CS-GO composite membrane was measured using a contact angle aberrometer (DSA-1, KRUSS). A Thermal Gravimetric Analyzer (TGA, METTLER TOLEDO) was employed to determine the proportion of each component of the MOF@CS composite materials.

Nanofiltration performance of MOF@CS-GO composite membranes

The nanofiltration (NF) properties of the membranes were evaluated using a cross-flow filtration device. Throughout the filtration procedure, the transmembrane pressure of all membranes was kept at 2 bar. The equipment was run for 30 min at 2 bar pressure until the membrane permeability reached a steady state. Then, 50 mg·L^{-1} of organic dye solutions (CR, MB, and crystal violet) were tested as the feed solution. The membrane had a test surface area of 4 cm^2. The permeance J (L·m^2·h^{-1}·bar^{-1}) is calculated by:

$$J = \frac{V}{AtP} \quad (1)$$

Table 1. Preparation conditions of MOF@CS-GO composite membranes

Membrane	0.01 wt% MOF@CS (mL)	0.0025 wt% GO (mL)
M1	0	1.0
M2	1.0	1.0
M3	3.0	1.0
M4	6.0	1.0
M5	3.0	2.0
M6	3.0	3.0

MOF@CS: Metal-organic framework@Chitosan; GO: graphene oxide.

Where V (L) represents the volume of permeate water; A (m^2) is the effective membrane area; t (h) is the permeation time; P (MPa) is the permeation pressure. The absorbance of the dye solutions in the wavelength range of 200-1,000 nm was measured by an ultraviolet (UV)-visible spectrophotometer (UV-400, Shimadzu), and the remaining concentration of the dyes in the permeate solution was calculated according to the standard curve. The retention rate R (%) of the dye was calculated based on:

$$R = \frac{C_f - C_p}{C_f} \times 100\% \quad (2)$$

Where C_f ($mg \cdot L^{-1}$) is the dye concentration in the feed solution, and C_p ($mg \cdot L^{-1}$) represents that in the permeate solution.

RESULTS AND DISCUSSION

Characterization of UiO-66-COOH and MOF@CS core-shell nanoparticles

From the XRD pattern [Figure 1A], the main peak positions of the prepared UiO-66-COOH nanoparticles were consistent with the simulated UiO-66 XRD pattern, indicating the successful synthesis of UiO-66-COOH. In addition, the characteristic peak of the UiO-66-COOH nanoparticles at $2\theta = 7°$-$9°$ was broader, indicating that the size of UiO-66-COOH particles is relatively small[40,41]. This is crucial for preparing MOF@CS-GO composite membranes with suitable interlayer spacing. The MOF@CS core-shell nanoparticles showed the same main peak position as UiO-66-COOH but a lower peak intensity, indicating that the CS enwrapped the UiO-66-COOH surface without destroying its structure.

The FTIR spectra of CS, UiO-66-COOH, and MOF@CS are shown in Figure 1B. The absorption peak of UiO-66-COOH at 1,402 cm^{-1} is attributed to C=C on the benzene ring of H_3BTC, while the absorption peak at 1,459 cm^{-1} is due to C–O vibration on the carboxyl group[42,43]. Furthermore, the peak observed at 658 cm^{-1} represents the Zr–O bond in UiO-66-COOH[30,44]. These results prove the successful synthesis of UiO-66-COOH nanoparticles[45,46]. For CS, the relatively strong peaks at 1,639 and 1,276 cm^{-1} can be attributed to the bending vibration of the -NH_2 group. For the MOF@CS core-shell nanoparticles, in addition to the characteristic peaks of CS and UiO-66-COOH, the C–N formed by the reaction of the carboxyl group with the amino group at 1,630 cm^{-1} was observed, indicating that CS was successfully cross-linked chemically with UiO-66-COOH[47,48].

TGA analysis was used to further characterize the MOF@CS sample. As shown in Figure 1C, the decomposition of CS was mainly observed at 225-420 °C, while the decomposition temperature of MOF is at 420-600 °C. For MOF@CS, the first weight loss at < 150 °C comes mainly from the evaporation of water. The second weight loss of 18% at 225-420 °C can be attributed to the decomposition of CS. The third weight loss of 10% at 420-600 °C is due to the decomposition of UiO-66-COOH[49-51].

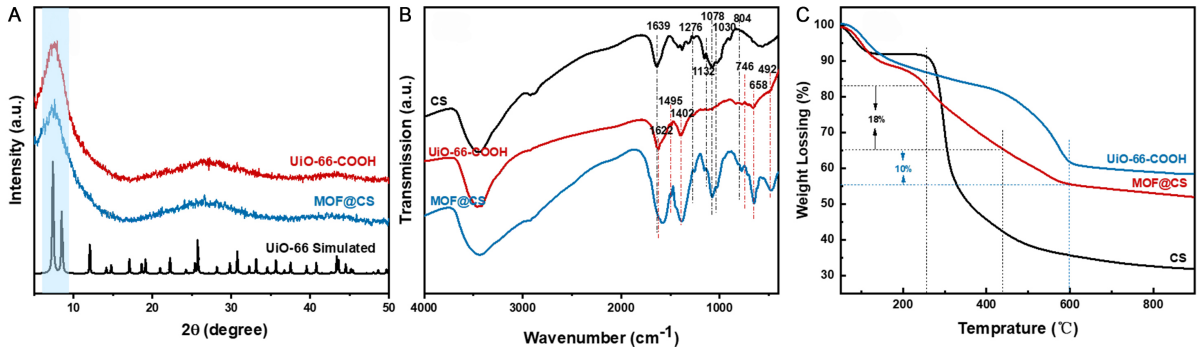

Figure 1. (A) XRD pattern; (B) FTIR; and (C) TGA diagram spectrum of CS, UiO-66-COOH, and MOF@CS core-shell nanoparticles. XRD: X-ray diffraction; FTIR: Fourier transform infrared spectroscopy; TGA: thermal gravimetric analyzer; MOF@CS: metal-organic framework@Chitosan.

The SEM analysis shows that the particle size of UiO-66-COOH is ~30 nm [Figure 2], while the particle size of MOF@CS core-shell nanoparticles is ~90 nm. The particle size of MOF@CS is significantly larger than that of UiO-66-COOH, further confirming that the MOF is encapsulated within a shell of CS.

The element distribution of UiO-66-COOH and MOF@CS core-shell nanoparticles was analyzed by energy dispersive spectrometer (EDS) element mapping [Supplementary Figure 1]. The results showed that C, O, and Zr were uniformly distributed in UiO-66-COOH [Supplementary Figure 1A], and the presence of Zr was attributed to a large amount of UiO-66-COOH. In addition, C, O, N, and Zr were distributed in MOF@CS core-shell nanoparticles [Supplementary Figure 1B]. The N was derived from the CS. The coexistence of N and Zr demonstrates that this MOF@CS aggregate contains CS and UiO-66-COOH. The EDS mapping results provide evidence for the successful synthesis of MOF@CS nanoparticles. The EDS mapping, combined with XRD and SEM results [Figure 1A and Figure 2], demonstrates the successful synthesis of core-shell structure MOF@CS nanoparticles.

Characterization of MOF@CS-GO composite membranes

MOF@CS-GO composite membranes with varying MOF@CS amount

A series of MOF@CS-GO composite membranes with different MOF@CS amounts and GO contents were prepared on PES substrates through vacuum filtration [Table 1]. The FTIR spectra of M1-M6 membranes are shown in Figure 3. The characteristic peaks around 1,917, 1,703, and 1,579 cm^{-1} can be assigned to the C=O and C=C functional groups in GO[52], respectively. The peak observed at 770 cm^{-1} represents the Zr–O bond in UiO-66-COOH, demonstrating that the MOF structure is retained[30,45,46]. The characteristic peaks at 1,650 and 1,680 cm^{-1} are attributed to the -CONH stretching vibration, implying that the functional groups in CS (-NH_2) have reacted with -COOH in GO[53,54]. The observation of the characteristic peaks of CS, GO, and UiO-66-COOH and their interaction peaks demonstrated the successful incorporation of MOF@CS core-shell nanoparticles into GO-based composite membranes.

Figure 4 shows the morphology characteristics of M1-M4 membranes. For the M1 membrane [Figure 4A], the macroporous PES substrate [Supplementary Figure 2] was not coated by the GO nanosheets completely and many holes of different sizes (marked by white circles) were on the surface. In contrast, with the increase of MOF@CS concentrations, the M2-M4 membranes became increasingly denser and without holes and obvious defects [Figure 4B-D], indicating that MOF@CS formed a continuous membrane. From the cross-sectional SEM images of the membranes [Figure 4E-H], their thickness with low MOF@CS content (M2) is about 110 nm and increases to 120 nm with the increase of the MOF@CS content (M4).

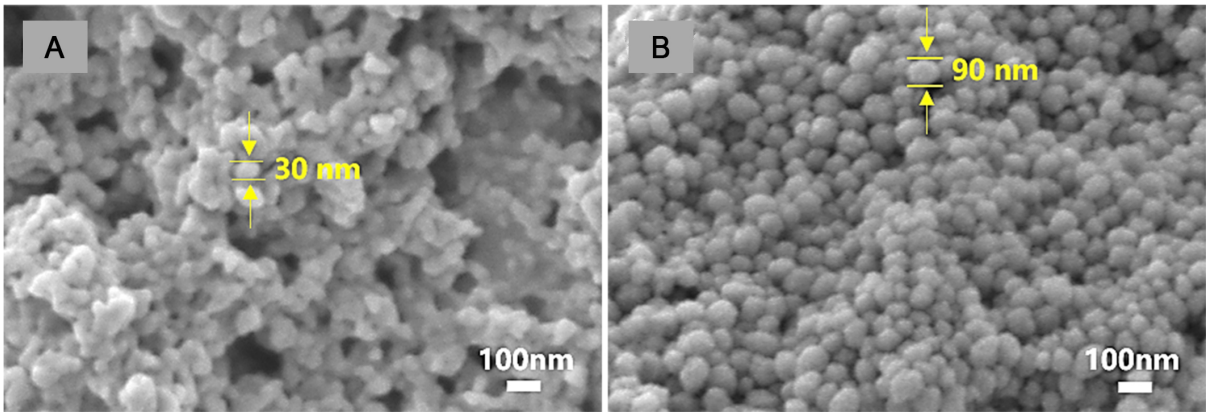

Figure 2. SEM images and of (A) UiO-66-COOH; and (B) MOF@CS core-shell nanoparticles. SEM: Scanning electron microscopy; MOF@CS: metal-organic framework@Chitosan.

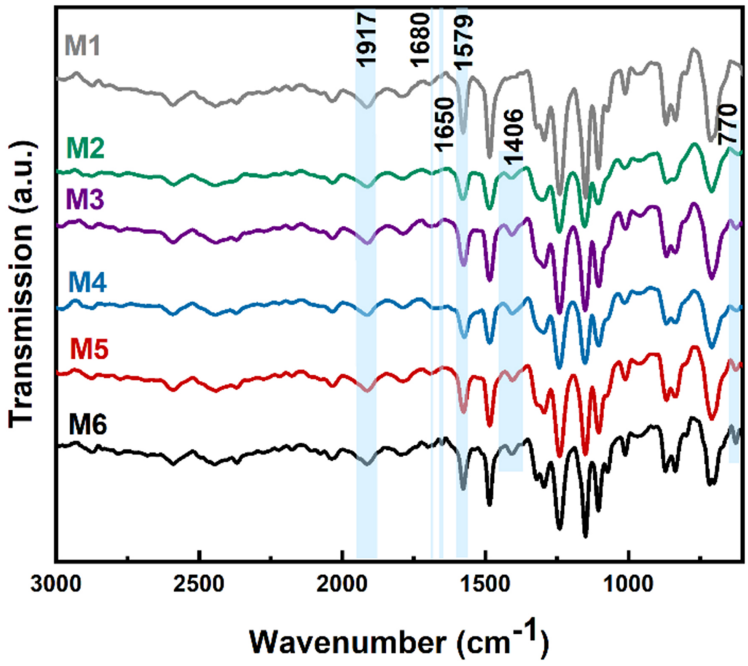

Figure 3. ATR-FTIR spectra of the GO (M1) and MOF@CS-GO (M2-M6) membranes. ATR-FTIR: Attenuated total reflection Fourier transform infrared spectroscopy; GO: graphene oxide; MOF@CS: metal-organic framework@Chitosan.

The surface roughness of the MOF@CS-GO membranes was characterized by AFM, and the results are summarized in Figure 5 and Table 2. The pure GO membrane has the smallest roughness (Ra = 12.9 nm, Rq = 17.775 nm), and the roughness for M2-M4 gradually increases with the inclusion of MOF@CS nanoparticles. The roughness variation is consistent with the surface morphology change of the MOF@CS-GO composite membranes.

Measuring the surface hydrophilicity of the membrane was essential as it reflects the hydrophilicity of the membranes. For this purpose, we utilized a water contact angle drop gauge [Figure 5E-H and Table 2] for M1-M4. The water droplets rapidly diffused on the surface of the M1-M4 membranes and then spontaneously penetrated the membranes, demonstrating the excellent hydrophilicity of the MOF@CS-GO

Table 2. Surface roughness parameters (Ra and Rq) of M1-M4 (a-d) were measured using AFM, and the initial contact angle and retention time of water on the membrane surface for M1-M4 (e-h)

Membrane	Ra (nm)	Rq (nm)	Contact angle (°)	Time (s)
M1	12.904	17.775	31.1 ± 1.4	4 ± 1
M2	16.781	20.986	32.0 ± 0.8	4 ± 1
M3	18.908	23.723	40.09 ± 0.5	6 ± 3
M4	22.240	29.024	46.1 ± 1.1	8 ± 2

AFM: Atomic force microscopy.

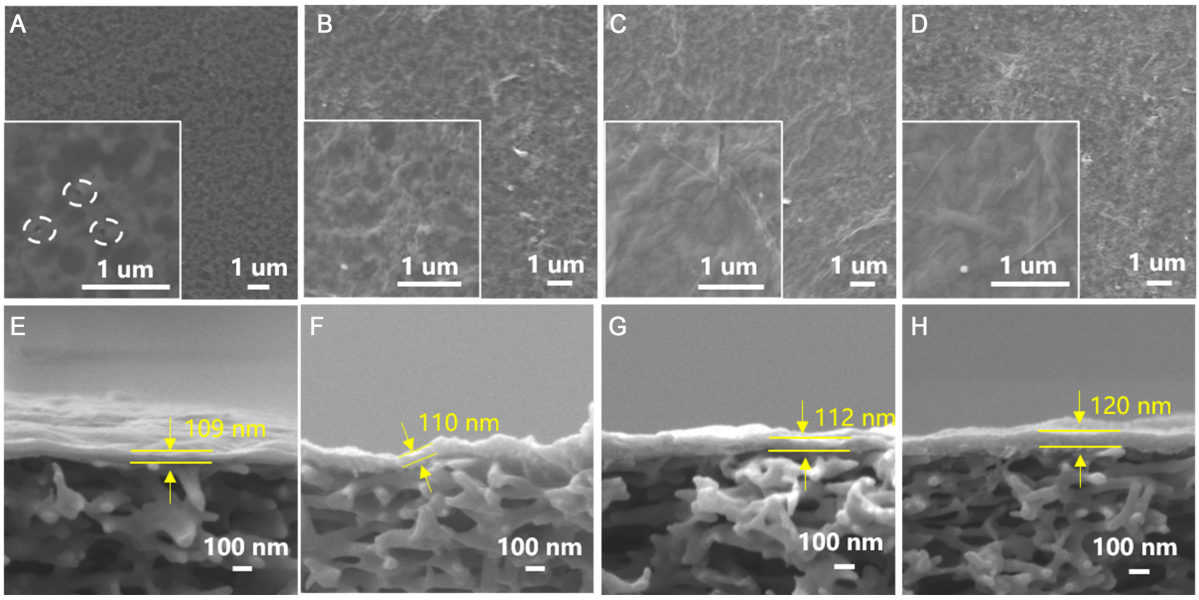

Figure 4. Top surface (A-D) and cross-sectional (E-H) SEM images of MOF@CS-GO membranes with different MOF@CS contents (M1-M4). SEM: Scanning electron microscopy; MOF@CS: metal-organic framework@Chitosan; GO: graphene oxide.

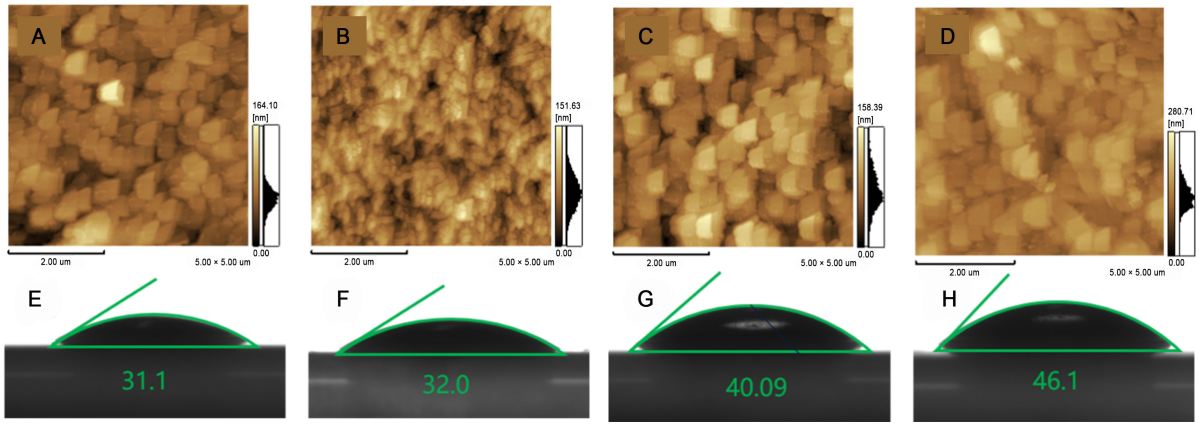

Figure 5. AFM images (A-D) and water contact angles of (E-H) MOF@CS-GO membranes with different MOF@CS contents (M1-M4). AFM: Atomic force microscopy; MOF@CS: metal-organic framework@Chitosan; GO: graphene oxide.

composite membranes. From M1 to M4, the initial contact angles are 31.1 ± 1.4, 32.0 ± 0.8, 40.09 ± 0.5, and 46.1 ± 1.1, respectively. The reduced water contact angle of M1 compared to M2 can be explained by the

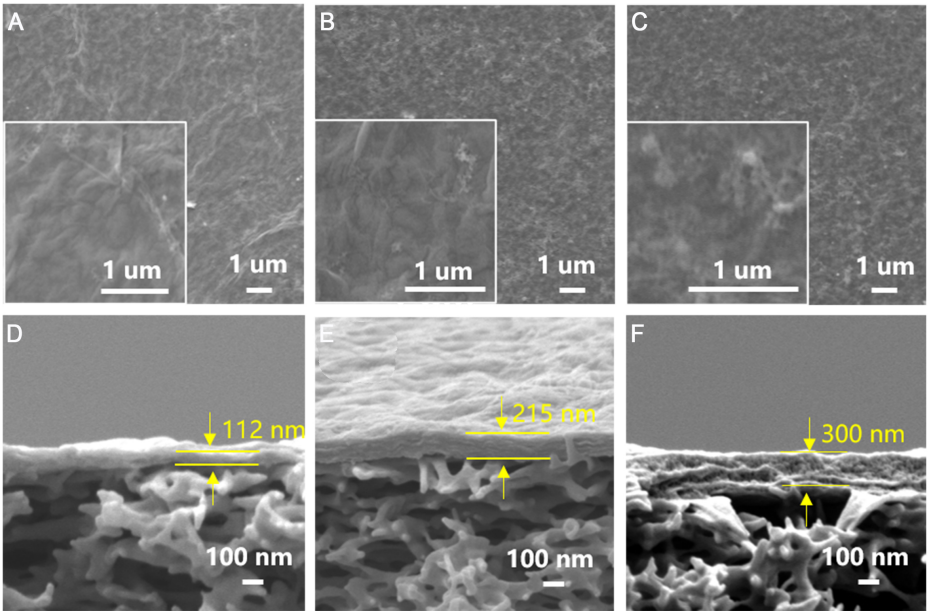

Figure 6. The top surface and cross-sectional SEM images of (A-F) MOF@CS-GO membranes with different GO contents (M3, M5, and M6). SEM: Scanning electron microscopy; MOF@CS: metal-organic framework@Chitosan; GO: graphene oxide.

presence of partial surface defects on M1, in accordance with the SEM image in Figure 4. For M2-M4, with the incorporation of MOF@CS nanoparticles, the contact angle showed an increasing trend. This is because the hydrophilicity of MOF@CS is weaker than that of GO [Supplementary Figure 3], resulting in the increase of the contact angle with higher MOF@CS content.

MOF@CS-GO composite membranes with varying GO amount

Figure 6 shows the morphology of a series of MOF@CS-GO composite membranes prepared with different GO contents and fixed MOF@CS content. With increasing GO content, the membrane surface becomes denser. Meanwhile, the wrinkling of GO can be seen from the enlarged images, indicating that GO covers a thin layer on the substrate surface. From the cross-sectional SEM images, the thickness of the membrane with a low GO content [M3, Figure 6D] is about 112 nm, and with increasing GO content, it increases to 300 nm [M6, Figure 6F]. The layered stacking structure of GO and the uniform dispersion of MOF@CS core-shell nanoparticles between the GO layers can be observed, proving that MOF@CS inserted the GO layer successfully.

The AFM results from Figure 7A-C and Table 3 show that the roughness of the membranes changes with the GO content. The higher the content of GO, the rougher the membrane surface becomes (M3, M5, M6). This is because, at high GO concentrations, the interaction force between GO and MOF@CS is strong, resulting in the aggregation of MOF@CS-GO composite particles. Consequently, there is an increase in the roughness of the formed membrane. The water contact angle was measured for MOF@CS-GO composite membranes with different GO contents to determine the hydrophilicity of the membranes [Figure 7D-F and Table 3]. With rising GO concentration, the contact angle slightly decreased, indicating that the hydrophilicity of the composite membranes increased. This is corresponding to the roughness variation results of M3, M5, and M6[55].

Table 3. Surface roughness parameters (Ra and Rq) of M3, M5, and M6 (a-c) were measured using AFM. And the initial contact angle and retention time of water on the membrane surface for M3, M5, and M6 (d-f)

Membrane	Ra (nm)	Rq (nm)	Contact angle (°)	Time (s)
M3	18.908	23.723	40.09 ± 0.5	4 ± 1
M5	18.945	23.748	40.0 ± 1.0	4 ± 1
M6	20.039	25.374	38.9 ± 0.5	6 ± 1

AFM: Atomic force microscopy.

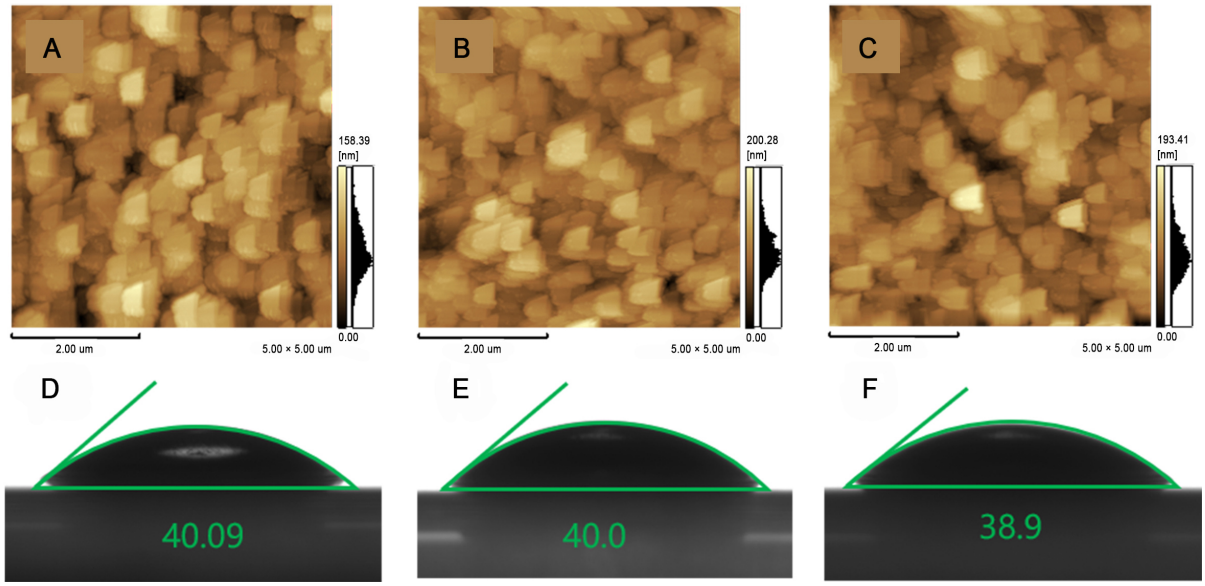

Figure 7. AFM images (A-C) and water contact angles (D-F) of MOF@CS-GO membranes with different GO contents (M3, M5, and M6). AFM: Atomic force microscopy; MOF@CS: metal-organic framework@Chitosan; GO: graphene oxide.

Nanofiltration performance of MOF@CS-GO composite membranes

The NF performance of a series of MOF@CS-GO composite membranes was evaluated in the staggered flow mode with CR. Firstly, the role of MOF@CS in the NF process of M1-M4 was confirmed [Figure 8A]. The permeance of M1 without MOF@CS was 738 $L \cdot m^{-2} \cdot h^{-1} \cdot bar^{-1}$, but due to the defects in the membrane, the CR rejection was only 76.5%. In contrast, the permeance of the M2 membrane decreased from 738 to 25.5 $L \cdot m^{-2} \cdot h^{-1} \cdot bar^{-1}$, but the rejection increased from 76.5% to 95.6%. This is because the pure GO membrane did not form a complete membrane in the absence of MOF@CS core-shell nanoparticles, which is consistent with the SEM results [Figure 4]. From M2 to M4, with the gradual increase of MOF@CS, the permeance of the MOF@CS-GO composite membrane goes through a maximum and then declines while the rejection remains relatively constant. This is attributed to the insertion of MOF@CS core-shell nanoparticles into the GO interlayer, which increases the interlayer spacing of GO, thereby enhancing the permeance of the composite membrane. However, the inherent resistance of the excessive MOF@CS particles limits the increase in water flux, hence the initial rise followed by a subsequent decrease in permeability[25].

In addition to MOF@CS, the influence of the GO amount on membrane performance has also been explored[56]. As shown in Figure 8B, the M3 prepared with low GO concentration had a high water permeance of 34.5 $L \cdot m^{-2} \cdot h^{-1} \cdot bar^{-1}$ and a rejection rate of 95.6%. As the GO concentration increased, the rejection for CR remained almost unchanged, but the permeance decreased significantly. This was primarily

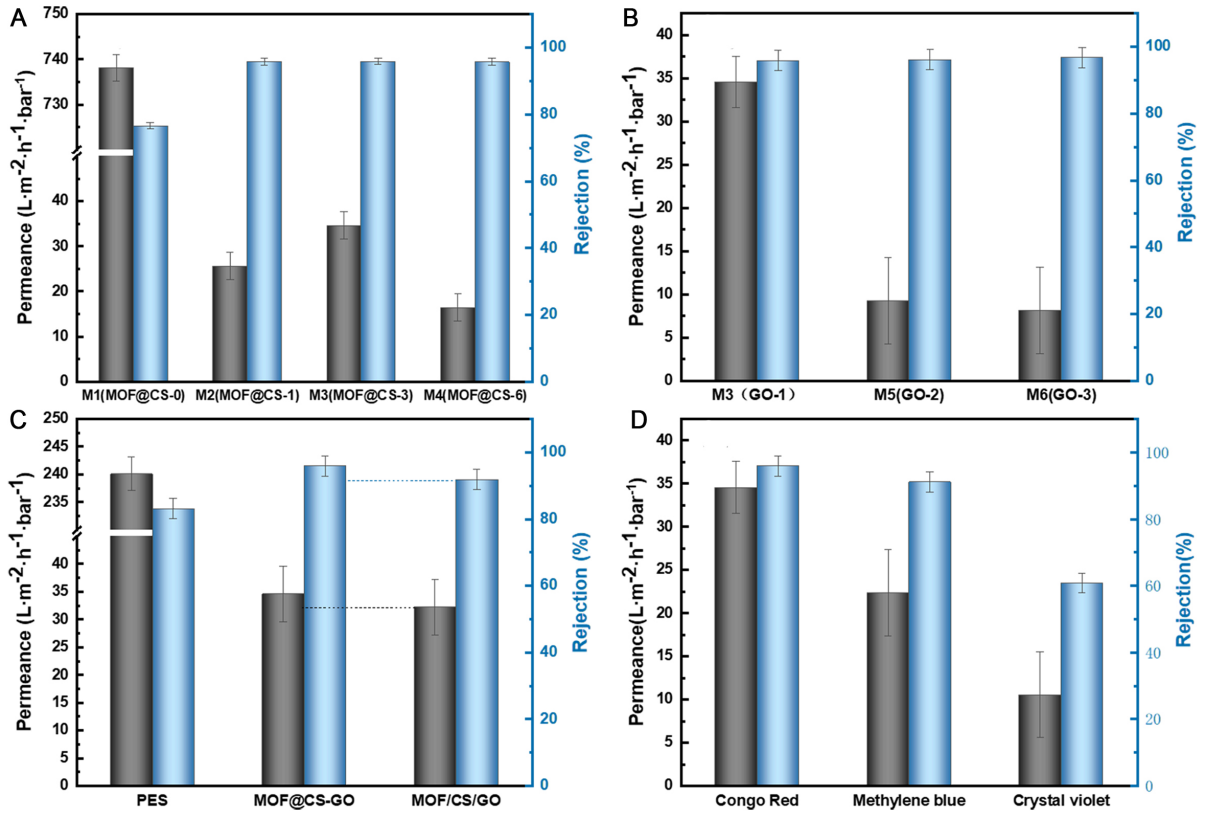

Figure 8. Effect of (A) MOF@CS and (B) GO concentration; (C) different membranes [PES substrate, MOF@CS-GO (M3) and MOF/CS/GO membrane]; and (D) different dyes on water permeability and dyes rejection rate. MOF@CS: Metal-organic framework@Chitosan; GO: graphene oxide; PES: polyethersulfone.

attributed to the rise in membrane thickness, which, in turn, increased the resistance to water transfer. Importantly, M3 has the best NF properties due to the effect of MOF@CS core-shell nanoparticles on the GO interlayer spacing. Therefore, in the subsequent performance exploration, we choose it as the representative of MOF@CS-GO to conduct a series of performance tests.

According to the TGA results at MOF@CS, as mentioned earlier, preparing MOF/CS/GO composite membranes involved physical mixing of equal proportions of CS and MOF. As shown in Figure 8C, the permeability and rejection rate of MOF@CS-GO composite membranes are higher than those of MOF/CS/GO composite membranes, indicating that GO composite membranes based on MOF@CS core-shell nanoparticles can improve the separation performance of GO membranes more effectively than the physical mixing of CS and MOF. To evaluate the NF performance of M3, several dyes with distinct charges and sizes, including crystal violet, MB, and CR, were used [Supplementary Table 1]. The rejection rates of M3 for CR, MB, and crystal violet aqueous solutions were 95.6%, 91.0%, and 60.6%, respectively [Figure 8D]. The MOF@CS-GO composite membrane exhibits a zeta potential of -22 mV at pH = 7 in aqueous solution [Supplementary Figure 4]. The negatively charged CR dye is almost completely rejected by the membrane, which is attributed to the effect of molecular sieving and electrostatic repulsion. However, the negative charge of the membrane partially attracts crystal violet with a positive charge, thus showing a relatively low rejection rate. The primary separation mechanism of MOF@CS-GO composite membranes is a combination of size exclusion and the Donnan effect. On the one hand, UiO-66-COOH, a novel class of porous crystalline materials, can effectively sieve dyes from water, while their nanometer-sized particle size

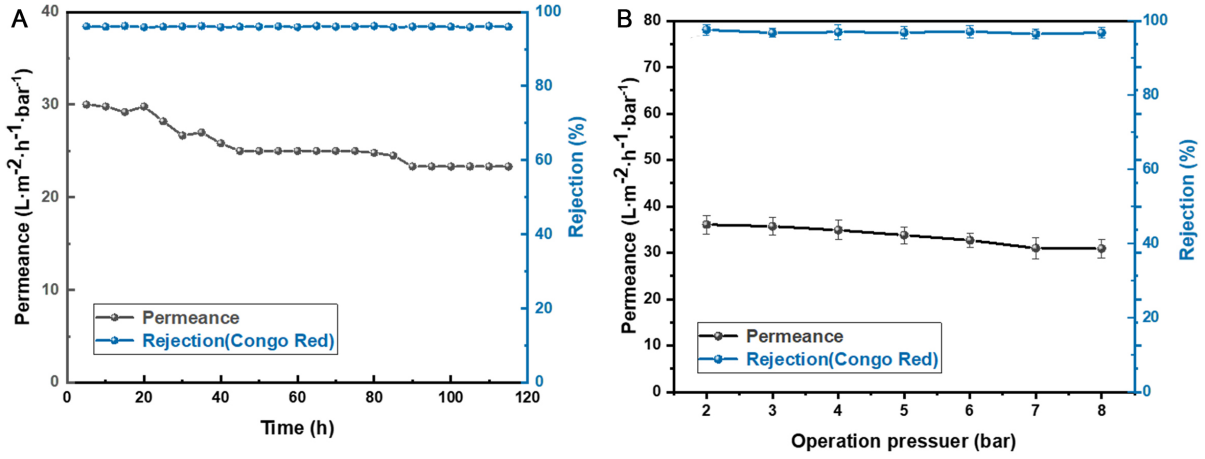

Figure 9. (A) Stability test of M3 with operating pressure of 2 bar and Congo red concentration of 50 mg·L^{-1}; and (B) pressure resistance test of M3 with increased pressure.

increases the layer distance of GO, which effectively improves the permeability of the membrane. On the other hand, cross-linking of CS can alleviate the non-selective voids between different species and the swelling problem of the GO layer, thus ensuring the stability of separation. Therefore, the MOF@CS core-shell structure formed by CS-wrapped MOF can improve the membrane permeability and rejection rate while maintaining its stability.

The long-term separation stability of M3 was assessed by evaluating its NF performance for 120 h [Figure 9]. M3 maintained a desirable rejection rate of 96% and a high water permeability of 25-30 L·m^{-2}·h^{-1}·bar^{-1}. This long-term stability of the membrane was attributed to the cross-linking effect of CS, where the amino functional group on CS and the carboxyl functional group on GO and MOF strongly interacted. In addition, the surface and edges of GO in aqueous solution are rich in oxygen-containing groups, which make GO negatively charged. Thus, positively charged CS can easily adsorb on the highly negatively charged surface of GO through electrostatic interactions, which, in turn, lead to GO being modified and prevented from restacking[57]. This covalent interaction tightly connects GO, CS, and MOF, enhancing the overall stability of the MOF@CS-GO composite membrane. As a result, the membrane can maintain its performance over an extended period.

Additionally, as can be seen in Figure 9B, the pressure resistance of the M3 was evaluated by assessing its NF performance at 8 bar. With increasing operating pressure, M3 maintained a desirable rejection rate of 96% and a high water permeance of 25-30 L·m^{-2}·h^{-1}·bar^{-1}. MOF intercalated into GO interlayer as a microporous filler can improve the mechanical stability of the composite structure and the pressure resistance of GO membranes[52].

The anti-pollution properties of the MOF@CS-GO composite membrane by filtrating a 50 μg/g bovine serum albumin (BSA) solution are illustrated in Figure 10. As the testing time increased, the water fluxes of the membrane gradually decreased. After conducting a two-hour BSA antifouling test on the MOF@CS-GO composite membrane, it was observed that the flux-decline ratio (FDR) was 50.5%. However, the decreased permeate can be partly regained by cleansing the membrane surface with pure water. The flux-recovery ratio (FRR) of the membrane was 77.5%, which is consistent with the structural properties of MOF@CS-GO membranes. The optimized surface charge resulting from the MOF@CS interlayer provides the membrane with enhanced antifouling propensity and cleaning ability.

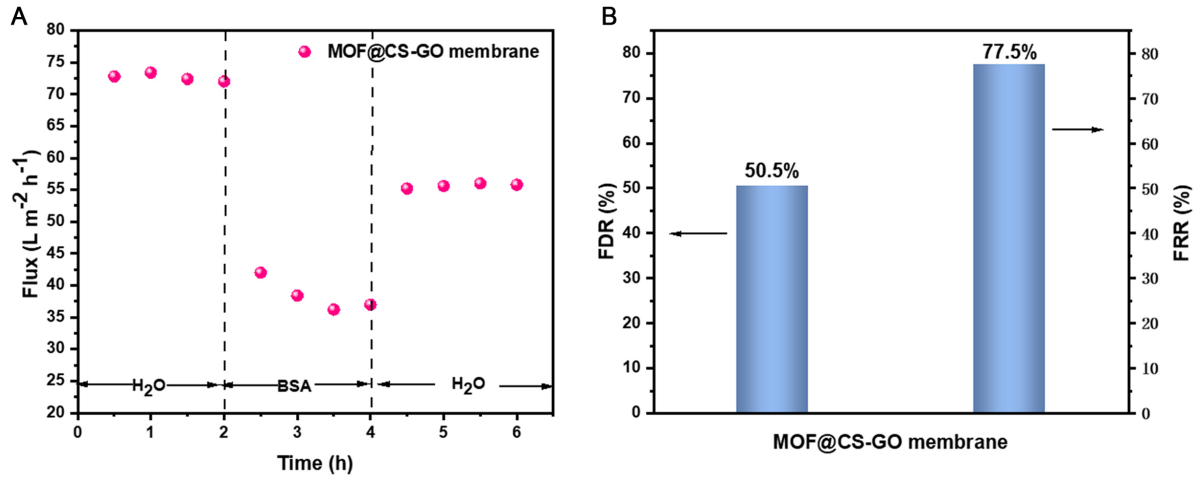

Figure 10. (A) The water flux variation; and (B) FDR and FRR of MOF@CS-GO composite membrane. FDR: Flux-decline ratio; FRR: flux-recovery ratio; MOF@CS: metal-organic framework@Chitosan; GO: graphene oxide.

Furthermore, as shown in Figure 11 and Supplementary Table 2, the performance of GO membranes with MOF@CS intercalation was also compared with other reported GO, CS, and MOF NF membranes. The comparison showed that the permeability and rejection of MOF@CS-GO composite membranes were superior to most NF membranes. Although the rejection of the MOF@CS-GO composite membranes can be further improved among the comparative membranes, their exceptional stability can greatly optimize their performance in practical applications. It is evident that these membranes exhibited excellent separation performance and stability.

Simulation of GO and MOF@CS-GO composite membranes

Molecular dynamics (MD) simulation was employed to investigate the water transport behavior in GO and MOF@CS-GO membranes [Figure 12 and Supplementary Figure 5] (see the details in Supplementary Materials for simulation). The mean square displacement (MSD) of water molecules in the two-channel models was calculated respectively [Figure 12A]. The results show that the MSD in the interlayer channel containing MOF@CS is higher than that of pure GO. Based on the Einstein relationship, the diffusion coefficients [Figure 12B] of the H_2O molecules in two transport channels were calculated from the MSD curves. The results showed that the diffusion rate of H_2O is 0.567×10^{-9} $m^2 \cdot s^{-1}$ in the pure GO membrane. In contrast, in the MOF@CS-GO membrane, it (1.713×10^{-9} $m^2 \cdot s^{-1}$) was three times higher than that of the pure GO membrane, which confirmed our predictions in the interpretation of the high permeability of MOF@CS-GO membranes.

CONCLUSIONS

To summarize, MOF@CS core-shell nanomaterials with dual regulatory effects were prepared and inserted into GO interlayers to optimize the separation performance, stability and pressure resistance of the GO membranes. As an intercalating agent, MOF@CS provided more permeation channels for the transport of H_2O molecules, while as a cross-linking agent, MOF@CS reduced the channel swelling between GO interlayers and effectively improved the stability of the membrane. The NF performance and stability of the improved MOF@CS-GO composite membranes were significantly enhanced. Compared to the pure GO membranes, the MOF@CS-GO composite membranes exhibited enhanced CR rejection rates (from 76.5% to 95.6%) while maintaining a high pure water flux (34.5 $L \cdot m^{-2} \cdot h^{-1} \cdot bar^{-1}$) and excellent structural stability (stable dye removal performance over 120 h). Implementing this dual regulation strategy is expected to

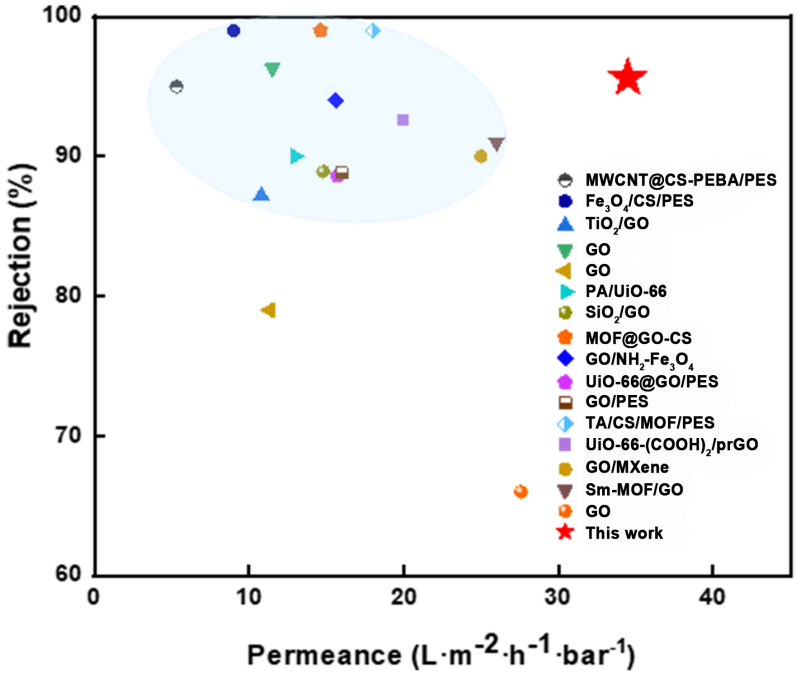

Figure 11. Comparison of nanofiltration performance between M3 with other reported results. The detailed date can be queried in Supplementary Table 2.

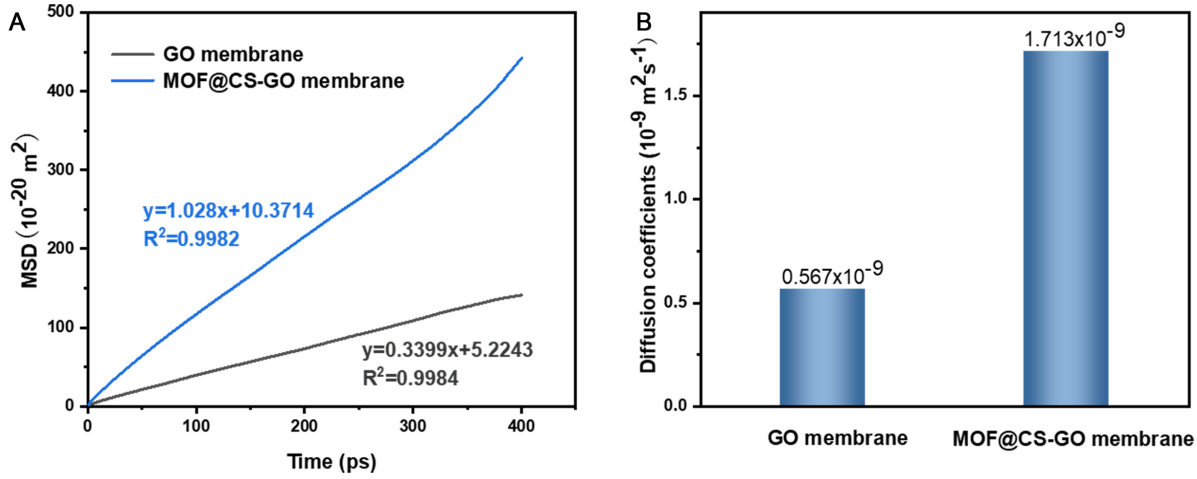

Figure 12. (A) The MSD of water molecules in the pure GO and MOF@CS-GO membranes; (B) The diffusion coefficients of the H_2O molecules in the pure GO and MOF@CS-GO membranes. MSD: Mean square displacement; GO: graphene oxide; MOF@CS: metal-organic framework@Chitosan.

effectively address the issue of GO membrane swelling in aqueous environments, presenting promising opportunities for developing high-performance GO membranes in water treatment applications.

DECLARATIONS

Authors' contributions

Made substantial contributions to the conception and design of the study, performed data analysis and interpretation, wrote the original draft, investigated the study, and performed data acquisition: Wang X

Made substantial contributions to the design of the study, performed data analysis and interpretation, and revised the manuscript: Cui X
Model construction and molecular dynamics simulation: Wang Z
Data analysis and interpretation: Zhang Z
Revised the manuscript and provided administrative, technical, and material support: Guo Y, Guo H, Tosheva L

Availability of data and materials
Not applicable.

Financial support and sponsorship
This work was financially supported by the National Key Research and Development Program of China of the Ministry of Science and Technology (2022YFE0116000), National Natural Science Foundation of China (No. 22175200 and No. 21975285), Fujian Province Science and Technology Program, Innovation Fund (2022C0021), Foreign cooperation project of Fujian Provincial Department of Science and Technology (2022I0044), Program for High-level Foreign Expert Introduction of China (G2023152003L), and Qingdao Municipal Natural Science Foundation of China (23-2-1-240-zyyd-jch).

Conflicts of interest
All authors declared that there are no conflicts of interest.

Ethical approval and consent to participate
Not applicable.

Consent for publication
Not applicable.

REFERENCES
1. Breedlove B, Weber JT. "No water, no life. No blue, no green". *Emerg Infect Dis* 2018;24:815-6. DOI PMC
2. Chen H, Yu X, Wang X, et al. Dyeing and finishing wastewater treatment in China: state of the art and perspective. *J Clean Prod* 2021;326:129353. DOI
3. Tkaczyk A, Mitrowska K, Posyniak A. Synthetic organic dyes as contaminants of the aquatic environment and their implications for ecosystems: a review. *Sci Total Environ* 2020;717:137222. DOI PubMed
4. Raza S, Ghasali E, Hayat A, Zhang P, Orooji Y, Lin H. Sodium alginate hydrogel-encapsulated trans-anethole based polymer: synthesis and applications as an eradicator of metals and dyes from wastewater. *Int J Biol Macromol* 2024;254:127153. DOI
5. Rojas S, Horcajada P. Metal-organic frameworks for the removal of emerging organic contaminants in water. *Chem Rev* 2020;120:8378-415. DOI PubMed
6. Raza S, Hameed MU, Ghasali E, et al. Algae extract delamination of molybdenum disulfide and surface modification with glycidyl methacrylate and polyaniline for the elimination of metal ions from wastewater. *Environ Res* 2023;221:115213. DOI
7. Bal G, Thakur A. Distinct approaches of removal of dyes from wastewater: a review. *Mater Today Proceed* 2022;50:1575-9. DOI
8. Zhang M, Sun J, Mao Y, Liu G, Jin W. Effect of substrate on formation and nanofiltration performance of graphene oxide membranes. *J Membrane Sci* 2019;574:196-204. DOI
9. Park TJ, Reznick J, Peterson BL, et al. Fructose-driven glycolysis supports anoxia resistance in the naked mole-rat. *Science* 2017;356:307-11. DOI PubMed
10. Gao Y, de Jubera AMS, Mariñas BJ, Moore JS. Nanofiltration membranes with modified active layer using aromatic polyamide dendrimers. *Adv Funct Mater* 2013;23:598-607. DOI
11. Peng X, Jin J, Nakamura Y, Ohno T, Ichinose I. Ultrafast permeation of water through protein-based membranes. *Nat Nanotechnol* 2009;4:353-7. DOI PubMed
12. Liu S, Wu C, Hung W, Lu X, Lee K. One-step constructed ultrathin Janus polyamide nanofilms with opposite charges for highly

efficient nanofiltration. *J Mater Chem A* 2017;5:22988-96. DOI

13. Qu H, Huang L, Han Z, et al. A review of graphene-oxide/metal-organic framework composites materials: characteristics, preparation and applications. *J Porous Mater* 2021;28:1837-65. DOI
14. Peng Y, Chen Z, Zhang R, et al. Oxygen-containing functional groups regulating the carbon/electrolyte interfacial properties toward enhanced K^+ storage. *Nanomicro Lett* 2021;13:192. DOI PubMed PMC
15. Otsuka H, Urita K, Honma N, et al. Transient chemical and structural changes in graphene oxide during ripening. *Nat Commun* 2024;15:1708. DOI PubMed PMC
16. Zhang WH, Yin MJ, Zhao Q, et al. Graphene oxide membranes with stable porous structure for ultrafast water transport. *Nat Nanotechnol* 2021;16:337-43. DOI
17. Fu H, Wang B, Zhu D, et al. Mechanism for selective binding of aromatic compounds on oxygen-rich graphene nanosheets based on molecule size/polarity matching. *Sci Adv* 2022;8:eabn4650. DOI PubMed PMC
18. Qiu L, Zhang X, Yang W, Wang Y, Simon GP, Li D. Controllable corrugation of chemically converted graphene sheets in water and potential application for nanofiltration. *Chem Commun* 2011;47:5810-2. DOI
19. Kim HW, Yoon HW, Yoon SM, et al. Selective gas transport through few-layered graphene and graphene oxide membranes. *Science* 2013;342:91-5. DOI
20. Dong L, Fan W, Tong X, Zhang H, Chen M, Zhao Y. A CO_2-responsive graphene oxide/polymer composite nanofiltration membrane for water purification. *J Mater Chem A* 2018;6:6785-91. DOI
21. Song X, Zambare RS, Qi S, et al. Charge-gated ion transport through polyelectrolyte intercalated amine reduced graphene oxide membranes. *ACS Appl Mater Interfaces* 2017;9:41482-95. DOI
22. Wang J, Zhang P, Liang B, et al. Graphene oxide as an effective barrier on a porous nanofibrous membrane for water treatment. *ACS Appl Mater Interfaces* 2016;8:6211-8. DOI
23. Hung W, An Q, De Guzman M, et al. Pressure-assisted self-assembly technique for fabricating composite membranes consisting of highly ordered selective laminate layers of amphiphilic graphene oxide. *Carbon* 2014;68:670-7. DOI
24. Zheng K, Li S, Chen Z, Chen Y, Hong Y, Lan W. Highly stable graphene oxide composite nanofiltration membrane. *Nanoscale* 2021;13:10061-6. DOI
25. Wu Y, Ye H, You C, et al. Construction of functionalized graphene separation membranes and their latest progress in water purification. *Sep Purif Technol* 2022;285:120301. DOI
26. Xu H, Ding M, Liu S, Li Y, Shen Z, Wang K. Preparation and characterization of novel polysulphone hybrid ultrafiltration membranes blended with N-doped GO/TiO_2 nanocomposites. *Polymer* 2017;117:198-207. DOI
27. Nguyen JG, Cohen SM. Moisture-resistant and superhydrophobic metal-organic frameworks obtained via postsynthetic modification. *J Am Chem Soc* 2010;132:4560-1. DOI PubMed PMC
28. Kitagawa S, Kitaura R, Noro S. Functional porous coordination polymers. *Angew Chem Int Ed Engl* 2004;43:2334-75. DOI PubMed
29. Cho KM, Lee HJ, Nam YT, et al. Ultrafast-selective nanofiltration of an hybrid membrane comprising laminated reduced graphene oxide/graphene oxide nanoribbons. *ACS Appl Mater Interfaces* 2019;11:27004-10. DOI
30. Fei L, Chen C, Shen L, et al. Graphene oxide assisted assembly of superhydrophilic MOF-based membrane with 2D/3D hybrid nanochannels for enhanced water purification. *Chem Eng J* 2023;460:141694. DOI
31. Jiang J, Wu D, Tian N, et al. Preparation of GO/GOH/MOFs ternary blend membrane and its application for enhanced dye wastewater purification. *J Solid State Chem* 2022;310:123028. DOI
32. Zeng H, Yu Z, Shao L, et al. A novel strategy for enhancing the performance of membranes for dyes separation: embedding PAA@UiO-66-NH_2 between graphene oxide sheets. *Chem Eng J* 2021;403:126281. DOI
33. Dong L, Li M, Zhang S, Si X, Bai Y, Zhang C. NH_2-Fe_3O_4-regulated graphene oxide membranes with well-defined laminar nanochannels for desalination of dye solutions. *Desalination* 2020;476:114227. DOI
34. Qian X, Li N, Wang Q, Ji S. Chitosan/graphene oxide mixed matrix membrane with enhanced water permeability for high-salinity water desalination by pervaporation. *Desalination* 2018;438:83-96. DOI
35. Ma H, Kong A, Ji Y, He B, Song Y, Li J. Ultrahigh adsorption capacities for anionic and cationic dyes from wastewater using only chitosan. *J Clean Prod* 2019;214:89-94. DOI
36. Lu Y, Zhang W, Wang M, Zhang H, Li J, Luo W. Fabrication of GO/PAN nanofiber membrane grafted with chitosan as efficient adsorbent for dye removal. *J Polym Environ* 2022;30:2943-54. DOI
37. Li Y, Zhao W, Weyland M, et al. Thermally reduced nanoporous graphene oxide membrane for desalination. *Environ Sci Technol* 2019;53:8314-23. DOI
38. Qian Y, Zhang X, Liu C, Zhou C, Huang A. Tuning interlayer spacing of graphene oxide membranes with enhanced desalination performance. *Desalination* 2019;460:56-63. DOI
39. Li L, Han S, Zhao S, Li X, Liu B, Liu Y. Chitosan modified metal-organic frameworks as a promising carrier for oral drug delivery. *RSC Adv* 2020;10:45130-8. DOI PubMed PMC
40. Kong G, Fan L, Zhao L, et al. Spray-dispersion of ultra-small EMT zeolite crystals in thin-film composite membrane for high-permeability nanofiltration process. *J Membrane Sci* 2021;622:119045. DOI
41. He HH, Yuan JP, Cai PY, et al. Yolk-shell and hollow Zr/Ce-UiO-66 for manipulating selectivity in tandem reactions and photoreactions. *J Am Chem Soc* 2023;145:17164-75. DOI
42. Jia X, Zhang B, Chen C, Fu X, Huang Q. Immobilization of chitosan grafted carboxylic Zr-MOF to porous starch for sulfanilamide

adsorption. *Carbohydr Polym* 2021;253:117305. DOI

43. Bumstead AM, Pakamorė I, Richards KD, et al. Post-synthetic modification of a metal-organic framework Glass. *Chem Mater* 2022;34:2187-96. DOI PubMed PMC
44. Luo J, Liu BS, Zhang XR, Liu RT. A Eu^{3+} post-functionalized metal-organic framework as fluorescent probe for highly selective sensing of Cu^{2+} in aqueous media. *J Mol Struct* 2019;1177:444-8. DOI
45. DeCoste JB, Peterson GW, Jasuja H, Glover TG, Huang Y, Walton KS. Stability and degradation mechanisms of metal-organic frameworks containing the $Zr_6O_4(OH)_4$ secondary building unit. *J Mater Chem A* 2013;1:5642. DOI
46. Yang J, Dai Y, Zhu X, et al. Metal-organic frameworks with inherent recognition sites for selective phosphate sensing through their coordination-induced fluorescence enhancement effect. *J Mater Chem A* 2015;3:7445-52. DOI
47. Hu SZ, Huang T, Zhang N, Lei YZ, Wang Y. Chitosan-assisted MOFs dispersion via covalent bonding interaction toward highly efficient removal of heavy metal ions from wastewater. *Carbohydr Polym* 2022;277:118809. DOI PubMed
48. Chang R, Ma S, Guo X, et al. Hierarchically assembled graphene oxide composite membrane with self-healing and high-efficiency water purification performance. *ACS Appl Mater Interfaces* 2019;11:46251-60. DOI
49. Cui X, Kang Z, Fan W, et al. Assembling ionic liquids in MOF "Monomer" based membranes to trigger CO_2/CH_4 separation. *Mater Chem Front* 2022;6:3555-66. DOI
50. Guo H, Liu J, Li Y, Caro J, Huang A. Post-synthetic modification of highly stable UiO-66-NH_2 membranes on porous ceramic tubes with enhanced H_2 separation. *Micropor Mesopor Mat* 2021;313:110823. DOI
51. Vahidi M, Tavasoli A, Rashidi AM. Preparation of amine functionalized UiO-66, mixing with aqueous *N*-Methyldiethanolamine and application on CO_2 solubility. *J Nat Gas Sci Eng* 2016;28:651-9. DOI
52. Pang J, Kang Z, Wang R, et al. Exploring the sandwich antibacterial membranes based on UiO-66/graphene oxide for forward osmosis performance. *Carbon* 2019;144:321-32. DOI
53. Linh PH, Do Chung P, Van Khien N, et al. A simple approach for controlling the morphology of g-C_3N_4 nanosheets with enhanced photocatalytic properties. *Diam Relat Mater* 2021;111:108214. DOI
54. Chidhambaram N, Ravichandran K. Single step transformation of urea into metal-free g-C_3N_4 nanoflakes for visible light photocatalytic applications. *Mater Lett* 2017;207:44-8. DOI
55. Ren X, Ji D, Wen X, et al. Graphene oxide membranes for effective removal of humic acid. *J Mater Res* 2022;37:3362-71. DOI
56. Tang MJ, Liu ML, Wang DA, et al. Precisely patterned nanostrand surface of cucurbituril[*n*]-based nanofiltration membranes for effective alcohol-water condensation. *Nano Lett* 2020;20:2717-23. DOI
57. Wang S, Gao Y. Effect of GO/CS/PbS nanocomposite films on tetraethyoxysilane sensing. *J Polym Res* 2016;23:109. DOI